Grain size effects on the infrared spectrum of mineral mixtures with dark components: New laboratory experiments to interpret low-albedo rocky planetary surfaces

G. Poggiali, L. Fossi, A. Wargnier, J. Beccarelli, J. R. Brucato, M. A. Barucci, P. Beck, M. Matsuoka, T. Nakamura, F. Merlin, et al.

A&A, 685, A14 (2024)
https://doi.org/10.1051/0004-6361/202347681

Astronomy & Astrophysics

Grain size effects on the infrared spectrum of mineral mixtures with dark components: New laboratory experiments to interpret low-albedo rocky planetary surfaces

G. Poggiali[1,2], L. Fossi[3], A. Wargnier[1], J. Beccarelli[4], J. R. Brucato[2], M. A. Barucci[1], P. Beck[5], M. Matsuoka[6], T. Nakamura[7], F. Merlin[1], S. Fornasier[1,8], M. Pajola[3], A. Doressoundiram[1], T. Gautier[1,9], and G. David[1]

[1] LESIA – Observatoire de Paris, Université PSL, CNRS, Université Paris Cité, Sorbonne Université, 5 place Jules Janssen, 92190 Meudon, France
[2] INAF – Astrophysical Observatory of Arcetri, largo E. Fermi no. 5, 50125 Firenze, Italy
e-mail: giovanni.poggiali@inaf.it
[3] Dipartimento di Fisica, Università degli Studi di Firenze, Via Sansone no. 1, 50019 Sesto Fiorentino (FI), Italy
[4] INAF – Astronomical Observatory of Padova, Vicolo dell'Osservatorio no. 5, 35122 Padova, Italy
[5] Univ. Grenoble Alpes, CNRS, IPAG, 38000 Grenoble, France
[6] The Geological Survey of Japan, National Institute of Advanced Industrial Science and Technology, Tsukuba, Japan
[7] Department of Geophysics, Tohoku University, Sendai Miyagi, Japan
[8] Institut Universitaire de France (IUF), 1 rue Descartes, F-75231 Paris Cedex 05, France
[9] LATMOS, CNRS, Sorbonne Université, Université Versailles St-Quentin, Guyancourt, France

Received 8 August 2023 / Accepted 22 December 2023

ABSTRACT

Context. A number of bodies in the Solar System are characterized by dark surfaces, from carbonaceous asteroids to the enigmatic surface of Phobos and Deimos. Our understanding of the spectroscopic behavior of low-albedo surfaces remains incomplete. To improve the interpretation of remote sensing data, laboratory studies continue to serve as a pivotal tool for unveiling the physical state and composition of such surfaces.
Aims. Several processes can be simulated in the laboratory, however, the preparation and analysis of a complex mixing of analog material is one of the most fundamental among them, while also being one of the most complex when multiple components are used. In this work, we aim to study how dark material mixed with basaltic material at different grain sizes can affect the spectroscopic features from the near- to mid- infrared (1.25–25 μm).
Methods. Our sample set includes four series of basaltic mix (feldspar and pyroxene) at different grain sizes from <50 μm to 1000 μm, mixed with amorphous carbon at increasing weight percentages ranging from 1% to 50%. We analyzed several features on the spectrum of each mineral mixture. In particular, we investigated the behavior of the: (i) near-infrared slope; (ii) 2.7 μm OH-stretching band; (iii) Christiansen features; and (iv) Reststrahlen band and Transparency feature.
Results. The measurements presented in this work, which take into account a large wavelength range for the first time, point toward a critical effect of dark material, but with a different outcomes for each grain size. Some of the most interesting results involve the slope trend of modification with dark material and the variant behavior of the Reststrahlen band and Transparency feature.
Conclusions. This dataset will offer a key support in the interpretation of data collected on dark surfaces by past and future space missions. This knowledge will be also important in the context of linking analyses of returned samples with remote sensing data collected on planetary surfaces.

Key words. methods: laboratory: solid state – techniques: spectroscopic – minor planets, asteroids: general – planets and satellites: composition – planets and satellites: surfaces

1. Introduction

Many rocky bodies of the Solar System, both large and small, are characterized by a low albedo, which affects the interpretation of surface composition by profoundly changing the spectroscopic appearance of these objects. Our current knowledge of how the physical properties influence the infrared (IR) spectrum is still incomplete. To note a few cases among known asteroids, the C-complex as well as the D-type are characterized by albedos lower than 0.1 (DeMeo & Carry 2013). Moreover, D-type asteroids have also been proposed as a possible origin (in the hypothesis of captured asteroids) for the Martian moons Phobos and Deimos, two objects that are among the darkest in the Solar System (Higuchi & Ida 2017). Although the most likely origin is a giant collision (Hyodo et al. 2017), this still does not explain their dark appearance. In general, a dark surface can be related to multiple factors attributable to some main classes: the presence of opaque material (Cloutis et al. 1990), strong surface alteration by space weathering (Hasegawa et al. 2022) or by thermal alteration (Lugassi et al. 2014), or shock darkening (Kohout et al. 2020). In various scenarios, the mixing of two components with very different mineralogy and origin can be observed, resulting in albedo values and grain sizes that vary considerably, as in the case of the exogenous material on asteroids (4) Vesta (Turrini et al. 2014), (101955) Bennu (DellaGiustina et al. 2021), and (162173) Ryugu (Tatsumi et al. 2021). This mixing of different

material will likely be observed also on dark surfaces from future space missions.

To unveil the properties of complex mixtures with dark components, laboratory studies are among the most powerful tools at our disposal. Regarding the study of spectroscopic features and the influence of grain size on the spectrum, numerous studies have been conducted in the past (e.g., Salisbury & Walter 1989; Salisbury & Wald 1992; Hiroi & Pieters 1992; Pieters et al. 1993; Mustard & Hays 1997; Cooper & Mustard 1999; Le Bras & Erard 2003; Piatek et al. 2004; Milliken & Mustard 2007; Sultana et al. 2021, 2023; Poggiali et al. 2023). Several main features are altered at different particle sizes: spectral slope, absolute reflectance values, and spectral contrast of absorption features (i.e., the band depth). Most bands show a monotonic decrease as particle size decreases with some exception for stronger bands, where the particle size variation induces the passage between volume scattering and surface scattering.

On the other side, some works have investigated the effect of adding dark and/or opaque components (e.g., Clark 1983; Cloutis et al. 1990) finding mostly effects on band area ratios and band widths. In Poggiali et al. (2022), we performed some preliminary experiments to investigate the mixtures of Martian simulants and carbonaceous chondrites simulants as effects of complex mixtures with different albedo components. Similar experiments were carried out in the attempt of matching Phobos spectrum by Wargnier et al. (2023a,b). All these previous studies, although they have mostly been working with only one grain size, agree that the presence of a dark component is a critical factor in suppressing the bands of the other mineralogical components in the near-infrared (NIR) range, but with a smaller effect in the mid-infrared (MIR) range.

Pommerol & Schmitt (2008) started the combined investigation between grain size and mixing with a dark component. In their work, smectite montmorillonite, volcanic tuff, and gypsum were mixed with anthracite (a mature, dry, and dark coal) while varying the grain size of the latter. More recently Bruschini et al. (2022) studied the behavior of mixtures of graphite with volcanic glass, gabbronite, and basalt, while changing the grain size of the bright component. Both papers focused on the visible (VIS) and NIR ranges, with the former concentrating on the 1.9 and 3 μm H2O absorption bands and the latter investigating the 0.35–2.5 μm range. For the first time, our work aims to extend the range to the MIR (up to 25 μm) using different material with respect to the previous studies. The results from the two papers are compared directly with our results in the discussion in Sect. 4.

2. Samples and methods

2.1. Preparation of mixtures

The mineral mixtures used in this work involved three components: two defined as "bright" bytownite and augite, along with a third "dark" component that is amorphous carbon. The two components were chosen for their distinctive spectrscopic appearance and diversity, we briefly discuss their possible link with planetary material in Sects. 4 and 5.

Bytownite $(Ca,Na)(Si,Al)_4O_8$ is part of feldspar mineral group in the plagioclase series, while augite $(Ca,Mg,Fe^{2+},Fe^{3+},Ti,Al)_2(Si,Al)_2O$ is a mineral of the pyroxene family (both characterized in Poggiali et al. 2023). Plagioclase and pyroxene were used in this work, always mixed together at 50/50 weight percentage [wt.%] with the same grain size. We give these two component samples the name of basaltic mixtures [BAS]. The opaque material, synthetic amorphous carbon [SAC], was produced in laboratory by arc discharge (Bussoletti et al. 1987; Colangeli et al. 1993).

In order to study the effect of darkening on different grain sizes in BAS samples, we need to select the grain size of pyroxene and plagioclase samples (<50 μm, 50–200 μm, 200–500 μm, and 500–1000 μm) and to mix them with SAC at different proportions (1, 5, 10, 30, and 50 wt.%). While the smaller percentages, such as 1 wt.% and 5 wt.%, are closer to realistic scenarios of the presence of carbon (particularly if we are considering carbonaceous meteorites or samples coming from space missions), the larger percentages were chosen to stress the conditions of the mix and observe changes on the spectrum under a wider range of proportions with a dark material.

To perform the preparation of the samples, we developed a protocol preliminarily introduced in Poggiali et al. (2023). The protocol consists of five phases presented below. The SAC sample was not passing through phase I, II, and III since it was already powdered, with a grain size of <150 μm.

– Phase I: crushing. Rock samples were separately milled using first an agate mortar and after a Retsch Planetary Ball Mills PM100 with an agate jar and two agate spheres to obtain fine dust.

– Phase II: sieving. The grounded samples of each mineral were sieved using the Retsch Vibratory Sieve Shaker AS200 in four selected ranges of: <50 μm, 50–200 μm, 200–500 μm, and 500–1000 μm. The sieving process is repeated two times: once dry and once with addition of ethanol in the sieves to enhance fine grains separation.

– Phase III: washing. After the mechanical sieving, samples with bigger grain sizes (50–200 μm, 200–500 μm, and 500–1000 μm) were additionally washed to remove smaller grain still present in the sample and still attached to bigger grain size particles thanks to electrostatic forces. Each selected sample is placed in a tall beaker with ethanol. The beaker is placed in an ultrasonic bath where the solution of ethanol and mineral is shaken to promote the removal of smaller grains attached to larger grains. A visible suspension of small grain size particles appears and after waiting for the larger grain sizes to fall to the bottom (i.e., time of the fall), the suspension is removed with a pipette. The time of fall is evaluated using the density of the mineral and the type of solvent. This procedure is repeated several times with addition of new pure ethanol until the suspension of small-sized grains disappears.

– Phase IV: mixing. The dried components are placed in an eppendorf tube and first mixed with spatula. After this step, a small quantity of ethanol is added to the tube in order to just cover the mineral mixtures, then the tube is placed 2 s in the ultrasonic bath to enhance mixing.

– Phase V: drying. All the samples were dried in the oven at max 50° C for 48 h to remove any traces of the solvent used and they were stored in the same oven before and after the IR measurements to avoid weather re-adsorption.

Preparing all the samples with this protocol assures an almost complete removal of small-sized grains from bigger ones. Using a scanning electron microscopy [SEM] analysis in the Process Engineering and Materials Laboratory [LGPM] laboratory at CentraleSupélec we looked for real grain sizes to check the effectiveness of the sieving process. As shown in Fig. A.1, the bigger grain sizes of augite and bytownite (Figs. A.1D to A.1F and A.1H to A.1J) do not show any small-sized grain contamination on the surface. Mechanical and ultrasonic mixing assure a preservation of endmembers original grain size and homogenous distribution

Table 1. Sample list.

Name	Description
SAC	Synthetic amorphous carbon
BAS-A	50/50 wt.% bytownite/augite <50 μm
BAS-B	50/50 wt.% bytownite/augite 50–200 μm
BAS-C	50/50 wt.% bytownite/augite 200–500 μm
BAS-D	50/50 wt.% bytownite/augite 500–1000 μm
MIX-01A	01 wt.% SAC + 99 wt.% BAS-A
MIX-01B	01 wt.% SAC + 99 wt.% BAS-B
MIX-01C	01 wt.% SAC + 99 wt.% BAS-C
MIX-01D	01 wt.% SAC + 99 wt.% BAS-D
MIX-02A	05 wt.% SAC + 95 wt.% BAS-A
MIX-02B	05 wt.% SAC + 95 wt.% BAS-B
MIX-02C	05 wt.% SAC + 95 wt.% BAS-C
MIX-02D	05 wt.% SAC + 95 wt.% BAS-D
MIX-03A	10 wt.% SAC + 90 wt.% BAS-A
MIX-03B	10 wt.% SAC + 90 wt.% BAS-B
MIX-03C	10 wt.% SAC + 90 wt.% BAS-C
MIX-03D	10 wt.% SAC + 90 wt.% BAS-D
MIX-04A	30 wt.% SAC + 70 wt.% BAS-A
MIX-04B	30 wt.% SAC + 70 wt.% BAS-B
MIX-04C	30 wt.% SAC + 70 wt.% BAS-C
MIX-04D	30 wt.% SAC + 70 wt.% BAS-D
MIX-05A	50 wt.% SAC + 50 wt.% BAS-A
MIX-05B	50 wt.% SAC + 50 wt.% BAS-B
MIX-05C	50 wt.% SAC + 50 wt.% BAS-C
MIX-05D	50 wt.% SAC + 50 wt.% BAS-D

of the components. Some examples of the results of the mixing process are showed in Fig. A.2. Given the study of the grain size effects in IR spectra is the main focus of this paper, we decided to avoid using a mortar that may reduce the grain size during mixing. The complete list of all the samples used in our analysis is reported in Table 1, along with details on the percentage of each mixture.

2.2. FTIR measurements and analysis

Fourier Transform InfraRed (FTIR) reflectance spectra were collected at the INAF-Astrophysical Observatory of Arcetri in Florence, Italy. Data were measured with a Bruker VERTEX 70v interferometer interfaced with Harrick Praying Mantis™ for the Diffuse Reflectance Infrared Fourier Transform Spectroscopy [DRIFTS] analysis in biconical 6:1, 90° off-axis ellipsoids mirror geometry. Elements used in the apparatus are: MIR Globar source, deuterated triglycine sulfate [DTGS] detector, and optical elements in KBr. This configuration allows measuring spectra on a wavenumber range between 8000 and 400 cm^{-1} (1.25–25 μm in wavelength) with 4 cm^{-1} spectral resolution and spot on the sample of approximately 3 mm. Each spectrum was the result of 100 scans of the interferometer. The Infragold® standard from Labsphere was used to acquire the reference background before each measurement session.

After preparation, all the mixtures were stored in the oven for the entire duration of the IR measurement session. Once the sample was placed in the Praying Mantis™, the sample chamber was evacuated with a turbomolecular pump with a minimum pressure attainable of 5×10^{-5} mbar. The sample was left in vacuum condition for 10 min prior to the spectrum acquisition to enhance the removal of adsorbed water. Each sample was measured three

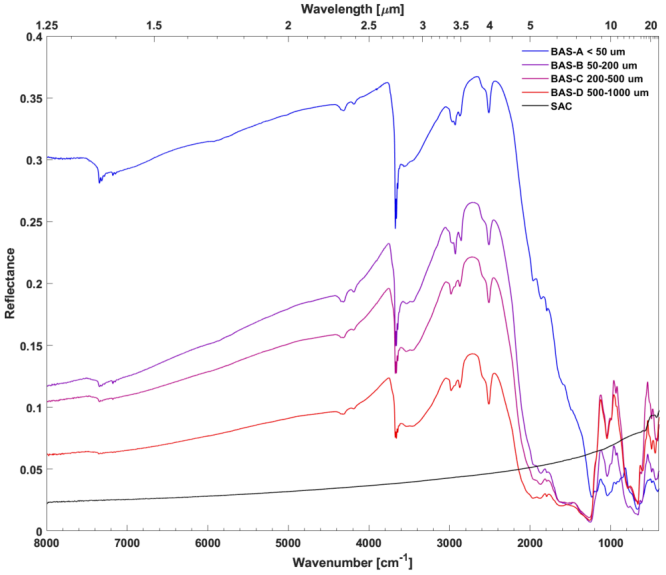

Fig. 1. IR spectra of basaltic mixtures at different grain sizes. From top to bottom: <50 μm, 50–200 μm, 200–500 μm and 500–1000 μm (from blue to red, respectively). The SAC spectrum is shown as a continuous black line at the lowest reflectance.

times: every time removing the quantity used from the sample holder, placing it back in the tube, mixing it with the rest of the sample, and re-measuring it anew. This procedure minimizes differences in the spectra that are due to inhomogeneities in the sample induced by mechanical (instead of intimate) mixing. This is particularly evident in larger sized grain mixtures. The three acquired spectra were then averaged into a final spectrum used for parameter evaluation. Errors were also derived from the three individual spectra as the maximum deviation from the mean value. The average final IR spectra of BAS, at any grain size and the SAC samples are shown in Fig. 1. Interestingly, although the minerals in the BAS sample are nominally anhydrous, a band at 2.7 μm related to the presence of OH in the structure is visible. This presence is related to OH defects in the structure that are present in many nominally anhydrous minerals (Righter 2007) and, in fact, the feature is characterized by multiple minima instead of a single broader troughs. Since the minima do not change their relative intensity, for this study, we limited ourselves to the first one in the band near 2.7 μm. In Figs. A.3 and A.4 are reported the spectra of the single components of BAS mixtures (augite and bytownite) at each grain size. Finally the reader can refer to appendix for all the single spectra measured in this work with the evaluated average. Figure A.5 shows all the spectra auto-scaled for the min-max reflectance and Fig. A.6 shows all the spectra reported, with the same reflectance scale for comparison.

For each spectrum, several parameters were evaluated in order to monitor and quantify the effect of addition of a dark component on complex samples with different grain sizes: (i) NIR slope between 1.5 and 2.5 μm; (ii) depth and band area for OH stretching band around 2.7 μm linked with water and OH content in the mineral matrix; (iii) CF minimum position linked with mineralogy and grain size; and (iv) peak intensity and band area for RB and TF in the MIR region, where the first is linked with the vibrational mode in the lattice of silicate minerals and the second generated by volume scattering effect in samples with small grain sizes. All these parameters were evaluated independently using a dedicated Matlab routine. More

details on the procedures to evaluate each parameter are reported in the appendix. In the next section, we present the IR spectra of the mixtures between BAS and SAC samples with the evaluated spectral parameters.

3. Results

From the combination of basaltic mixtures [BAS] in four different grain sizes with amorphous carbon [SAC] in five proportions, we obtained 24 spectra, listed in Fig. 2. The addition of SAC induces several changes in every feature of the spectrum from NIR to MIR range. These changes combine with the well-known modification induced by grain size reduction, such as slope reddening, as well as changes in the reflectance level and band contrast (Hunt & Vincent 1968; Arnold & Wagner 1988; Cloutis et al. 2018). We refer to Fig. A.7 for reflectance values in our dataset. Modifications can be observed in our dataset by comparing spectra between different BAS samples with the same percentage of SAC (i.e., different panel of Fig. 2). From the point of view of the appearance of spectral features, the spectra of the four BAS samples are very similar taking into account the heterogeneities due to the use of natural materials and the mechanical and non-intimate mixing technique. The BAS-A sample with grain sizes of <50 μm shows the characteristic Transparency features at about 12 μm (around 830 cm^{-1} in wave numbers) as expected from samples with small grain sizes (Salisbury et al. 1991).

With a first general comparison of the spectra, we can see that the MIR part of the spectrum, beyond the Christiansen minimum at 7–8 μm, is less affected in terms of absolute reflectance, but the presence of the SAC component leads to a reduction in spectral contrast. On the other hand, the NIR part of the spectrum, along with a reduction in spectral contrast, visible reductions in reflectance level are visible, especially for the smaller grain sizes of BAS-A and BAS-B. In detail, the sample at grain sizes of <50 μm BAS-A, with the addition of 10% SAC, reduces its reflectance much more than samples at bigger grain size such as BAS-D (500–1000 μm). The same absolute reflectance at 1.25 μm (spectrum acquisition limit) of the 50% mix between BAS and SAC changes between grain sizes of <50 and 500–1000 μm of about a factor of 2. In particular, the reflectance of BAS-A is 0.061±0.006, while the reflectance of BAS-D is 0.029±0.004. Later in this section, we discuss the major features of the spectrum individually and consider how various mix proportions affect their appearance.

3.1. Slope

Figures 3A–D show the details of the spectra of the mixtures between 1.25 and 2.6 μm normalized to 1.5 μm. Using the formula presented in the analysis method section in the appendix, we calculated the slope between 1.5 and 2.5 μm for each final spectra. Using the triplets of individual spectra, we calculated the corresponding slope errors; these are shown in Figs. 3E–H. Since our data from this dataset covered the SAC mixing percentage from 1% to 50% and the pure 100% SAC sample, we added data from our previous work Poggiali et al. (2022), where mixtures between the BAS and SAC at 50%, 70%, and 90% were present. The grain sizes of the bright samples used in the previous work are <200 μm. Notably, the value of the 50% mix slope realized in the previous paper agrees very well with the value of the mixtures measured in this new work (apart from sample BAS-B), pointing toward a reliability of the result obtained. If we examine the trend of the values we can generally see that the addition of a dark component such as SAC, characterized by low albedo, but not displaying a strong red slope as with other components, leads to a nonlinear trend. Furthermore, we observe decreasing values of the slope with increasing percentage of dark component followed by an increasing trend in the opposite direction. The percentage required to skip between the decreasing and increasing trend varies between 10% and 50%, depending on the BAS grain size. This particular trend is further discussed in Sect. 4.

3.2. Hydrated band

A second feature analyzed in detail in our study is the OH-vibrational band with a minimum around 2.7 μm. As observed in the method section, this band is likely due to OH defect in the structure of nominally anhydrous mineral constituents of the BAS samples (augite and bytownite). However, this band is due to OH stretching and, thus, it is structural of the mineral samples and it allows us to study its behavior in the presence of a dark component to generally apply it to features found in hydrated minerals. In Fig. 4, we can observe the behavior of the band in the continuum removed IR spectrum (Figs. 4A–D), the band area trend between 2.6 μm and 3.5 μm (Fig. 4E), and the minimum depth trend at 2.72 μm (Figs. 4F–I).

The band area and minimum depth generally show trends that are in agreement, as can be seen by comparing Fig. 4E, where all band area trends are reported with Figs.4F–I, where band depth trends for various grain sizes are shown individually. It is also interesting to note that modifications of this feature changes with increasing percentage of dark SAC components. The trend in terms of the modification of the band area and minimum depth is not the same as the grain size of the BAS sample changes. The smaller grains show a power law trend with more intense reduction even at lower SAC percentages. On the opposite side, by increasing the BAS grain size the trend tends to become more linear, as can be observed for BAS grain sizes of 200–500 and 500–1000 μm. For comparison, the OH band depth for BAS-A at grain sizes of <50 μm with the addition of 10% SAC is reduced by 57%, while the same percentage of SAC in the BAS-D sample with grain sizes of 500–1000 μm causes a 13% reduction. It is also observed, from the general comparison, that for very high percentages at 50%, the smaller grain sizes (BAS-A and BAS-B) experience a 75–85% reduction in band depth, while for the larger sizes (BAS-C and BAS-D), the band depth reduction is higher than 95%.

3.3. Christiansen features

The position of CF was determined for each spectrum in every grain size at any percentage of SAC mixing. The value of the minimum position for the CF was obtained by searching the minimum position for each spectrum of the same sample. This method leads to small errors when the minimum is well defined (BAS-A and BAS-B), but the errors increase when the CF is broader and less defined. All the results are shown in Figs. 5A–D, with the detail of the CF range in the spectrum, along the mean value of CF for each grain size highlighted as a dashed black vertical line. We observe, as previously reported in literature (Salisbury et al. 1987), that when increasing the grain size, the CF becomes broader at smaller wavelengths, this broadening also affects the evaluation of the spectrum relative minimum inducing larger errors. In Fig. 5E, we reported the position of the CF for each BAS sample (at different grain sizes) against the percentage of amorphous carbon.

Despite some larger errors in the larger sized grain mixtures, the value of the CF seems not to change drastically adding the

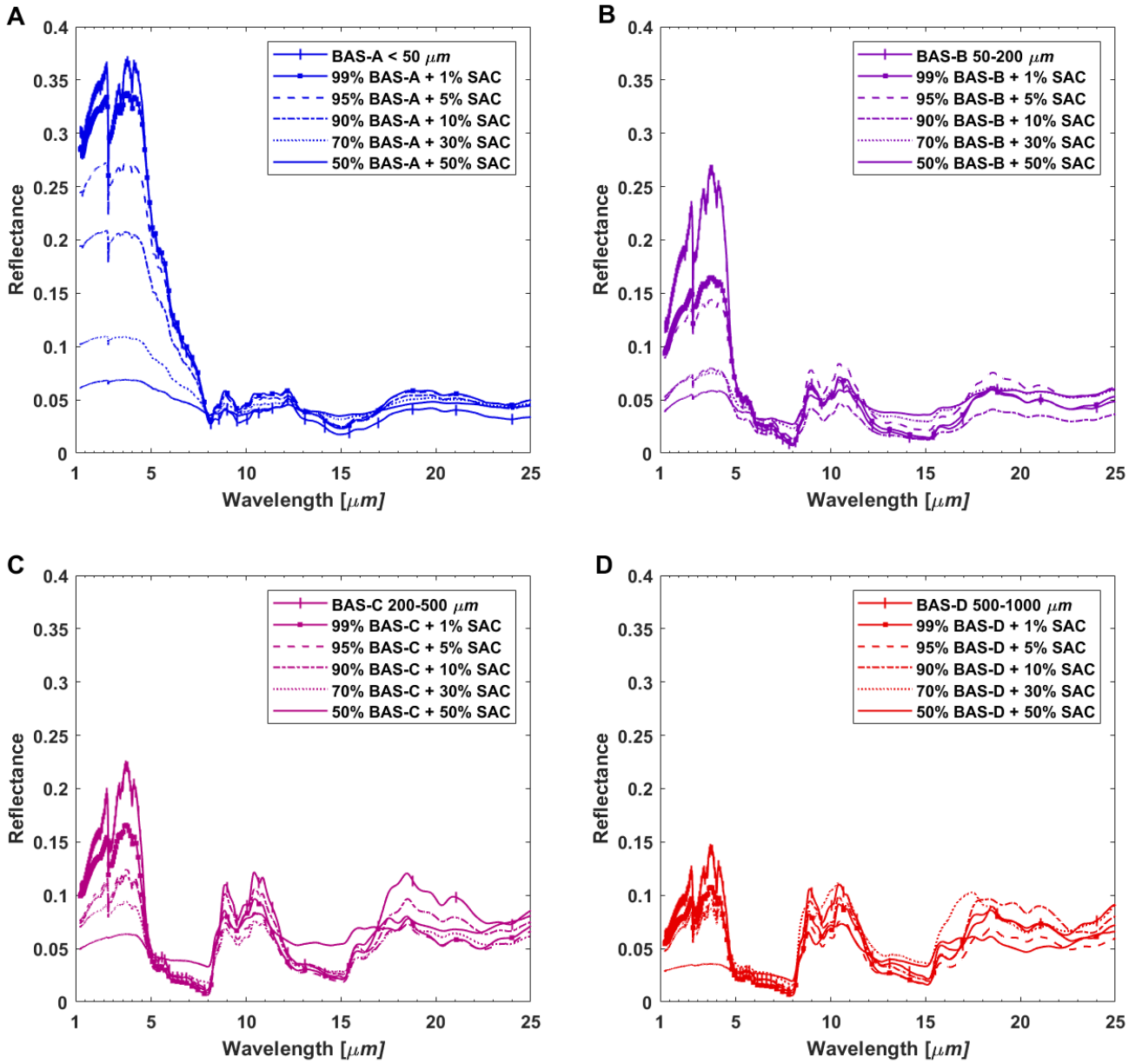

Fig. 2. IR spectra of basaltic mixtures [BAS] at different grain sizes in different proportions with synthetic amorphous carbon [SAC]. Top left panel: <50 μm; top-right panel: 50–200 μm; bottom-left panel: 200–500 μm; and bottom-right panel: 500–1000 μm. The mixture with different proportion of SAC are represented in each panel with continuous line with dash marker (0%), continuous line with a dot marker (1%), dashed line (5%), dashed-dotted line (10%), dotted line (30%), and pure continuous line (50%). The intensity scale is the same for each panel to enhance the difference in reflectance level among the four mixture combinations.

dark component SAC. We observe that the CF varies between the different BAS samples as expected by the difference in grain size; in the discussion in the next section, we compare this variation with some data from the literature. In Fig. 5E, we also report the weighted arithmetic mean of all the measurements at each grain size as a dashed line with values on the right axis. We found a shift in the mean value of CF for BAS-A and BAS-D of 0.16 μm. All the evaluated values and errors for CF are reported in Table 2.

3.4. Reststrahlen and transparency bands

We move on to the analysis of the MIR spectral range between 7.5 and 15.5 μm where, in addition to the already presented CF, we found RB and TF. In Figs. 6A–D, the continuum-removed spectrum between the CF position of each BAS sample and 15 μm is shown for all the samples. The vertical black lines with the label highlight the position used to evaluate the strength of RB in each BAS sample; we note that the adopted positions are reported in Table A.1, while the variation in the peak intensity for each sample with an increasing percentage of a dark component is shown in Figs. 6F–I. Since RB position for each BAS sample does not vary significantly between the mixtures with different percentages of SAC, we decided to use the same position for each spectrum. The natural variability is accounted for in the error associated with each value. We also measured the band area using the same limits of the continuum removal (CF position to 15.5 μm), with results reported in Fig. 6E.

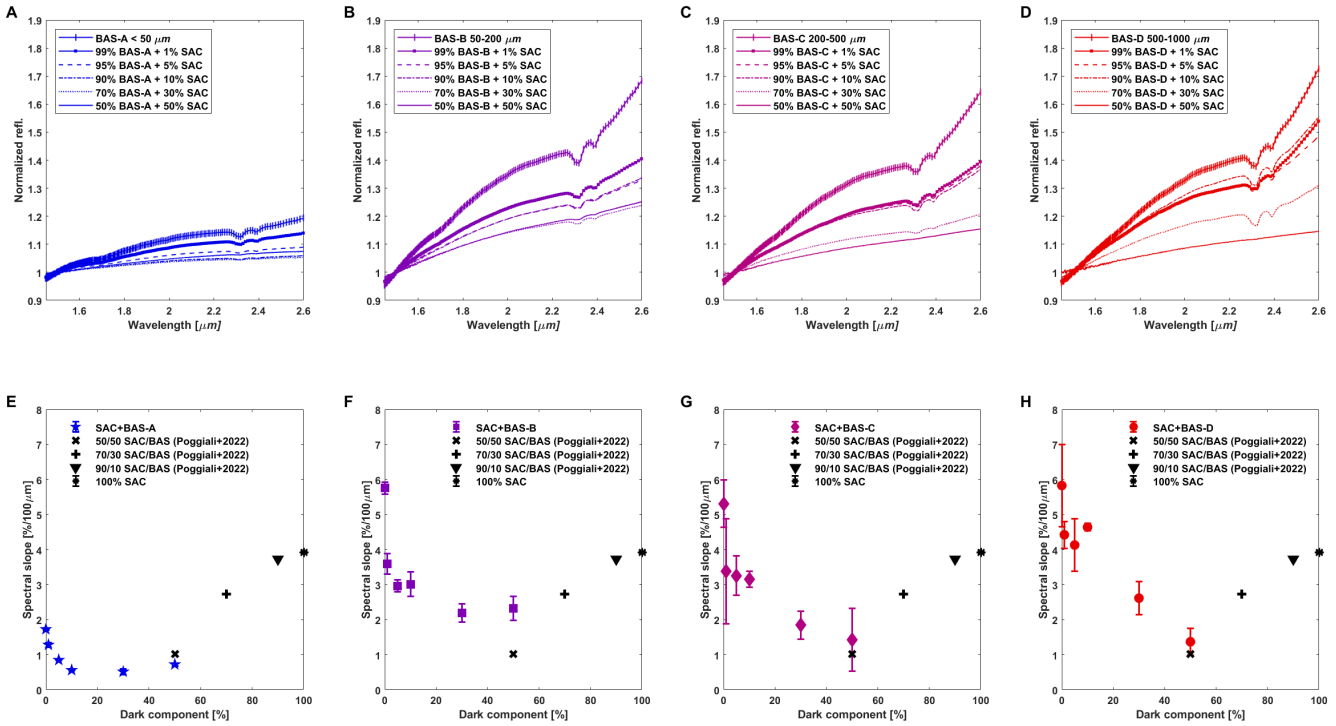

Fig. 3. Slope evaluation for the mixtures studied in this work. Panels A, B, C, and D: IR spectra normalized at 1.5 μm of basaltic samples [BAS] at different grain sizes (<50, 50–200, 200–500 and 500–1000 μm) mixed in different proportions (from 1 to 50%) with synthetic amorphous carbon [SAC], spectra are limited in the range 1.4–2.6 μm. Panels E, F, G, and H: values of the slope against percentage of SAC dark component for each mixture with errors. The black cross, plus, and triangle markers are the value of the slope for mixture at 50%, 70%, and 90%, respectively, from Poggiali et al. (2022). The black star marker is the value of the slope of pure SAC. Note: the samples at 50%, 70%, and 90% have a grain size that is comparable to that of sample SAC-A (<50 μm).

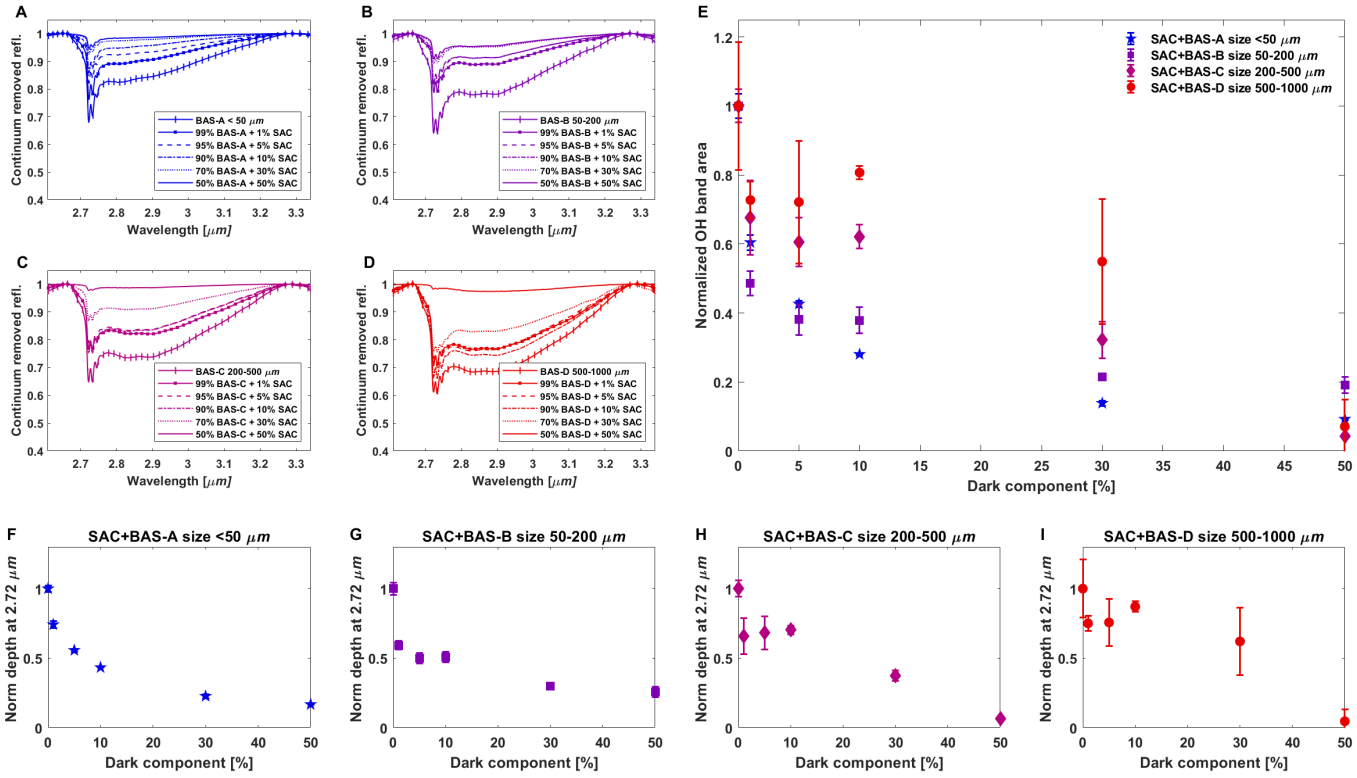

Fig. 4. Continuum-removed IR spectra of basaltic samples [BAS] at different grain sizes (<50, 50–200, 200–500, and 500–1000 μm) mixed in different proportions (from 1 to 50%) with synthetic amorphous carbon [SAC], spectra are limited in the range 2.6–3.3 μm to highlight the OH band at 2.7 μm, shown in panels A, B, C, and D. Panel E: band area, normalized at the value of pure BAS samples, evaluated for each series of mixing. Panels F, G, H, and I: depth of the minimum at 2.72 μm normalized at the value of pure BAS and evaluated for each series of mixtures.

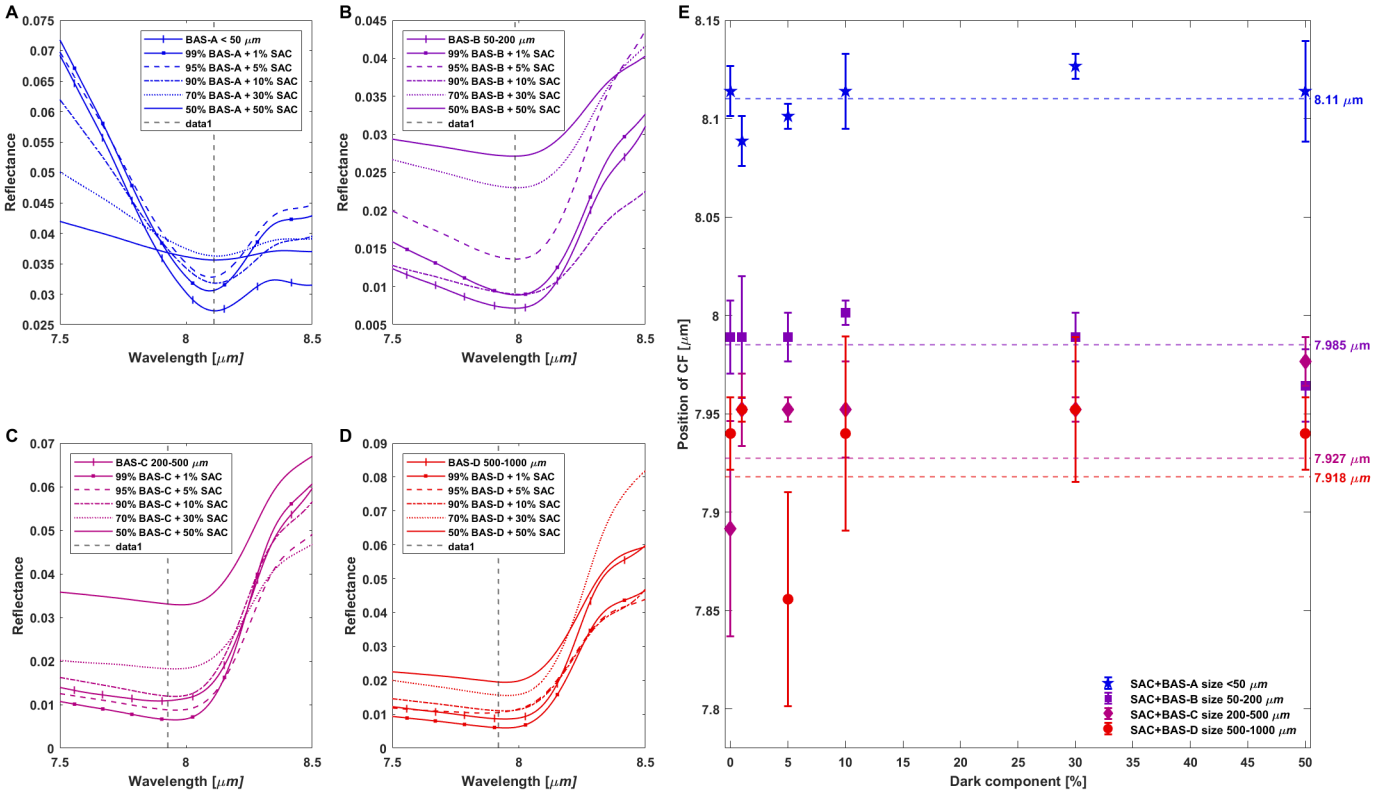

Fig. 5. IR spectra of basaltic samples [BAS] at different grain sizes (<50, 50–200, 200–500, and 500–1000 μm) mixed in different proportions (from 1 to 50%) with synthetic amorphous carbon [SAC], spectra are limited in the range of 7.5–9.5 μm to highlight the CF position, shown in panels A, B, C, and D. The average value for each grain size is represented by the vertical dashed black line. Panel E: Position of each mixture with different percentage of dark material. Dashed horizontal lines and the label on the right show the average value of the CF position for each BAS sample series.

Table 2. CF measured values.

Sample	CF position (μm)						
	PURE	+1% SAC	+5% SAC	+10% SAC	+30% SAC	+50% SAC	Mean value
BAS-A	8.11 ± 0.01	8.09 ± 0.01	8.101 ± 0.006	8.11 ± 0.02	8.127 ± 0.006	8.11 ± 0.02	8.11 ± 0.02
BAS-B	7.98 ± 0.01	7.98 ± 0.03	7.98 ± 0.01	8.001 ± 0.006	7.98 ± 0.01	7.96 ± 0.02	7.99 ± 0.02
BAS-C	7.89 ± 0.05	7.95 ± 0.02	7.95 ± 0.006	7.95 ± 0.02	7.95 ± 0.006	7.97 ± 0.01	7.95 ± 0.03
BAS-D	7.93 ± 0.02	7.95 ± 0.006	7.86 ± 0.05	7.94 ± 0.05	7.95 ± 0.04	7.94 ± 0.02	7.95 ± 0.04

In general, all the samples of BAS at different grain sizes show a decrease in band area (Fig. 6E) and peak intensity (Figs. 6F–I) with increasing proportion of SAC component in the mixtures. Among the different series of mixtures only BAS-B shows a regular decreasing trend especially in the low percentage mixtures (1–10%), while the three other BAS sample series are more irregular in the same percentage range and also have larger associated errors. The variability observed in the lower percentages may also be partly due to heterogeneity in the BAS sample. We discuss these differences in the next section.

Along with the RB, we also studied the TF in the BAS-A sample series and the results are shown in Fig. 7. For the evaluation of TF band area and peak height, we chose to remove the continuum and evaluate the area between 9.6 and 14.9 μm in order to reduce the influence of the first peak of RB around 8.9 μm. Although this modification was made for the analysis of this feature, a clear RB peak is still visible around 10.53 μm and several other shoulders are present around the TF at 12.25 μm; indeed the band area is not limited to the TF alone but also includes influence from the RBs. To understand how this overlap of peaks might affect the results, we evaluated not only the variation of the TF peak as the percentage of SAC increases, but also the intensity of the RB peak at around 10.5 μm. The results for the change in band area and relative intensity of the two peaks are shown in Fig. 7B at the bottom. It is evident how the band area is largely influenced by TF with a similar decreasing trend with respect to TF peak height. Both the parameters decrease with the addition of small percentages of SAC, while RB presents a more linear trend. The differences become smaller with the addition of dark component. For instance, at 5% SAC in the mix, the TF peak height decreases by 35% and the RB height by about 9%; conversely, as the percentage of SAC increases to 30%, the reduction amounts to 63% and 43%, respectively.

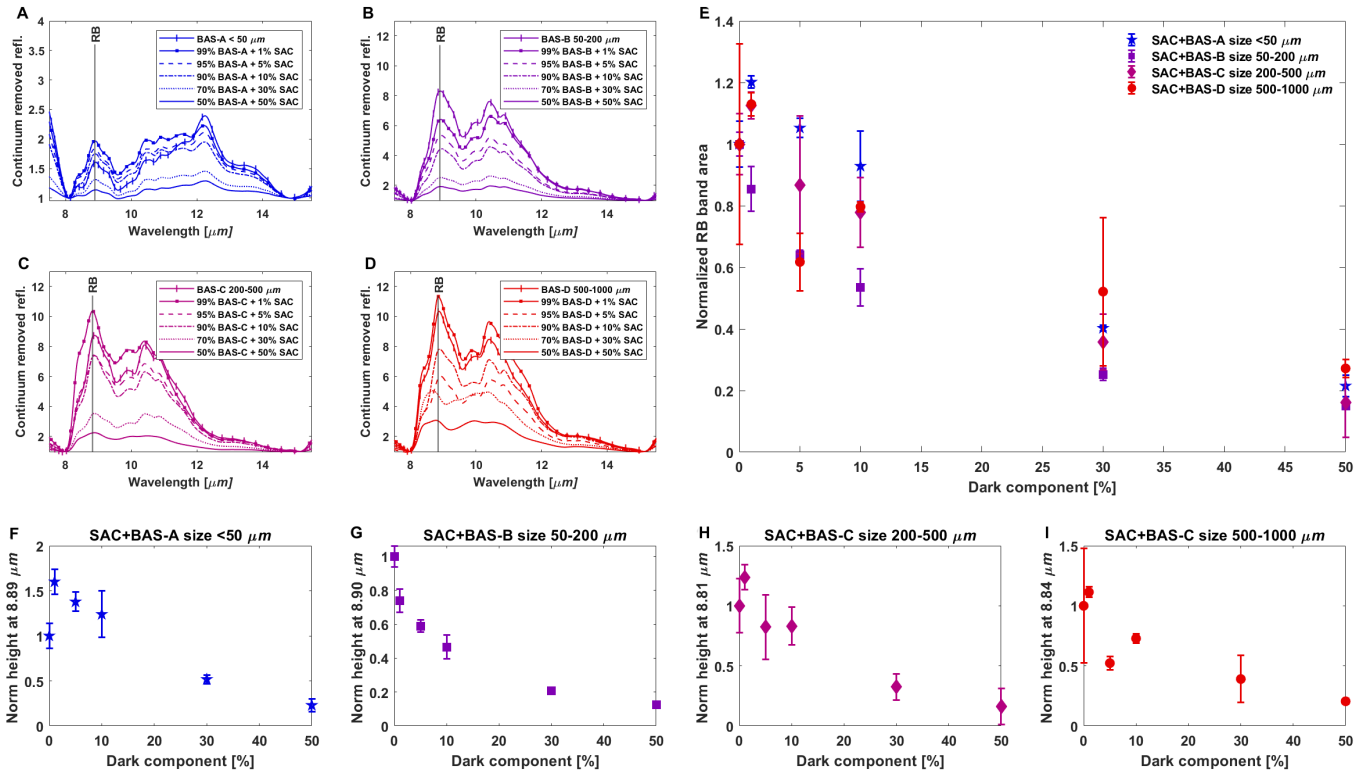

Fig. 6. Continuum-removed infrared spectra of basaltic samples (BAS) at different grain sizes (<50, 50–200, 200–500 and 500–1000 μm) mixed in different proportions (from 1 to 50%) with synthetic amorphous carbon [SAC], spectra are limited in the range 7.5–15.5 μm to highlight the RB region, shown in panels A, B, C, and D. Panel E: band area, normalized at the value of pure BAS samples, evaluated for each series of mixing. Panels F, G, H and I: height of the peak of RBs normalized at the value of pure BAS and evaluated for each series of mixtures (see Table A.1 for the precise wavelength and method used for peak depth evaluation).

4. Discussion

4.1. Discussion on laboratory results

The results presented above attempt to give a broader understanding of the effect of a dark component on different basaltic mixtures of different grain sizes. A first general observation that carries strong implications for the interpretation of observations can be made focusing on the reflectance level. We evaluated the reflectance values at 1.25 μm (the shortest wavelength available for our spectra) for each dimension of BAS samples at any mixing percentage, with a dark component SAC (results shown in Fig. 8). As is known from the literature, both for bright and dark components, different grain sizes are associated with different reflectance levels with decreasing reflectance for increasing grain size (Milliken & Mustard 2007; Cloutis et al. 2018). In agreement with previous works, as visible in Fig. A.7, the reflectance in our spectra changes by about five times for grain sizes from <50 μm to 500–1000 μm. When the dark component is added to the different grain sizes, the sample reflectance levels start to decrease as visible in Fig. 8. For 50% of SAC in the mixture, the reflectance values for all the samples notably fall within the range between 0.03 and 0.06, with difference between the smallest and biggest grain sizes is about two-fold, while for 30% SAC, the reflectance values for all the largest grain size samples (BAS-B, BAS-C, and BAS-D) fall within the range between 0.054 and 0.07, with BAS-A being 1.4 times greater than the rest. Looking at a 5% SAC, the reflectance of the same sample with larger grain sizes covers a range between 0.054 and 0.09 with BAS-A more than 2.5 times higher in reflectance. Indeed, looking at a homogenous surface in terms of composition, variations in albedo may be related to grain size. If the dark component does not vary in size, it is possible to easily discern spectroscopically between bright regolith size with 30% of the composition comprised of a dark component.

Moving to the analysis of the slope, some interesting results appear from our experiments, as visible in Figs. 3E–H: all the four series of mixtures at different grain sizes present a similar trend for the slope at increasing percentage of dark material. Sultana et al. (2023) observed a similar trend in their measurements: mixing olivine with iron sulfide FeS or anthracite at a hyperfine (<1 μm) grain size, they found that NIR slope progressively became bluer (negative slope) reaching a minimum value at 10 vol% of FeS and anthracite and for larger quantities it increased toward the value of the pure dark component. Bruschini et al. (2022) did not observe the trend in most of their samples, but their mixing percentage was limited up to 5%. Our samples used a bright component (basaltic mix) that presents a redder slope, but the trend is clearly comparable to that observed by Sultana et al. (2023). A decreasing slope for increasing the percentage of dark components and (passed over a threshold value for the percentage of dark components) the trend turns towards a more positive slope. Interestingly, the grain size used in our work is much larger than the previous studies and this led to different behavior of the trend. For grain sizes of <50 μm, the minimum value of the slope corresponds to about 20–30% of dark component, while increasing the grain size, the "minimum" position shifts toward a bigger percentage of amorphous carbon: 30–40% for grain sizes of 50–200 μm, about 40–50% for grain sizes of 200–500 μm, and 50% (or more) for grain sizes of 500–1000 μm. Unfortunately, our old

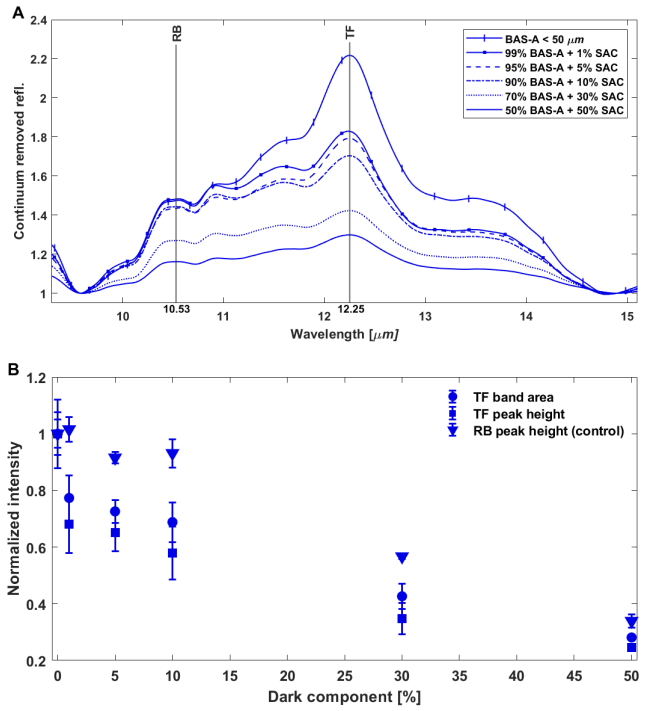

Fig. 7. Continuum-removed IR spectra of BAS-A sample mixed in different proportions (from 1 to 50%) with synthetic amorphous carbon [SAC], spectra are limited in the range 7.5–15 μm to highlight the TF band region, shown in panel A. Panel B: TF band area along with TF and RB peak height, normalized at the value of pure BAS-A samples, evaluated for each percentage of SAC added to the mixtures.

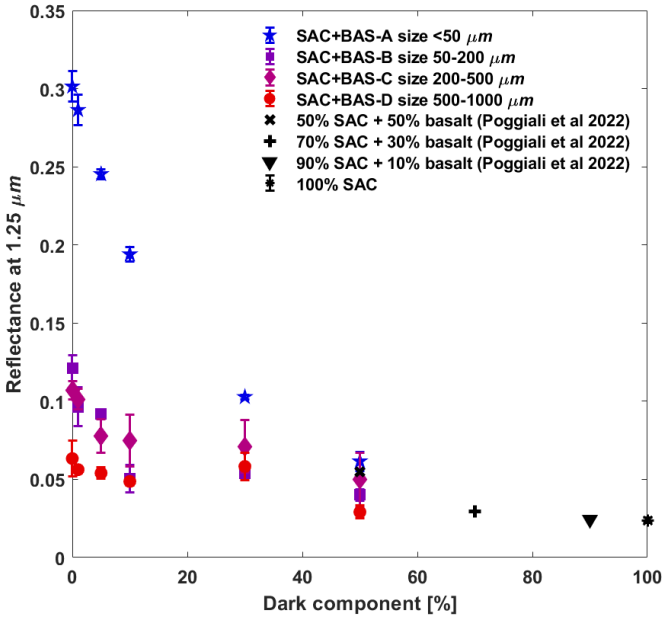

Fig. 8. Reflectance at 1.25 μm for basaltic samples [BAS] at different grain sizes (<50, 50–200, 200–500, and 500–1000 μm) mixed in different proportions (from 1 to 50%) with synthetic amorphous carbon (SAC). The black cross, plus and triangle marker are respectively the reflectance values for mixture at 50%, 70%, and 90% from Poggiali et al. (2022). The black star marker is the value of reflectance of pure SAC. Note: the samples at 50%, 70%, and 90% have a grain size that is only comparable to that of sample SAC-A (<50 μm).

data for higher percentages of carbon (50, 70, 90, and 100%) are adequately comparable only with the BAS-A size, but new data acquired in other series of measurements still allow us to observe a shift in the position of the threshold between blueing and reddening for the slope. The initial blueing is not related to the dark material composition. Indeed, we note that the effect is observed in the dataset we presented and with different opaque material in Sultana et al. (2023). Moreover, this effect of bluing of VIS and NIR spectrum due to small grains was observed in several Solar System environments (Clark et al. 2008; Yang et al. 2009; Brown et al. 2010). Brown (2014) theoretically found that a narrow size distribution of spherical scatterers will cause spectral bluing regardless of their optical index n, and therefore independent from the composition. For small quantities at small grain sizes, the effect of well-dispersed opaque particles induces bluing through individual scattering of light (Sultana et al. 2023). If the percentage of dark material increases, the opaque grains start to agglomerate (as visible in Fig. A.2) and they are no longer scattering in a Rayleigh regime. Interestingly, in our dataset we observe that by increasing the dimension of the grains of the bright material (that act as a separator of dark particles) the percentage needed to skip from blueing to reddening is higher. A possible explanation to this observation is related to the arrangement of small grains in the presence of large grains. As observed in previous laboratory experiments as well (Poggiali et al. 2023), small grains mixed with large grains tend to stick to the surface of the latter by electrostatic bonding. The larger the surface area of the bright grains, the higher the number of dark grains that can be accommodated on the surface before creating agglomerates. Therefore, as we observe in the various series of samples at different grain sizes, the percentage of opaque material required to find the threshold of the slope between blueing and reddening increases for bigger grain sizes. This result could be important in the context of predicting the amount of dark components we can expect on different brighter grains.

As visible in Figs. 4A–D, the 2.7 μm OH band in our sample presents a complex multi-troughs shape. Both augite and bytownite are anhydrous minerals and, in a pure form, they should not contain OH. Either way (as known from the literature), nominally anhydrous minerals especially when dealing with natural samples can contain OH defects in matrix (Righter 2007). Thus, being a structural band and not due to adsorbed water, we have the opportunity to study the behavior of these features in the presence of dark amorphous carbonaceous material. However, we must point out that it is not representative of a pure hydrated silicate and can only give a general idea of a similar effect on an OH band due to total hydration of a mineral. Figures 4E and F–I show, respectively the integrated band area and normalized peak depth for each BAS series at an increasing percentage of dark material. We noticed that, both for band area and peak depth, two different variation trends appear with different grain sizes: for samples of <200 μm the trend is not linear, while it tends to be more linear for bigger grain sizes of the bright component. Results on OH from our measurements can be directly compared with Pommerol & Schmitt (2008) study, the trend observed varying the grain size of the dark component is really in agreement with our results although the passage from between a linear and nonlinear trend is obtained with a 100 μm grain size for the dark material. In the same paper, the authors compare exhaustively their results to radiative transfer modeling and we refer to the original paper for more details and a full explanation of the observed phenomenon. However, in analogy with the

result obtained for the slope, it can be hypothesized that the different trends observed between small and large bright grains are related to the relative size of the dark component on the light one. Since the BAS grains are larger, the formation of SAC clumps on the surface may be delayed and require larger percentages.

Regarding the variation of the CF, our results demonstrate that most of the variation of this spectroscopic feature ought to be linked with grain sizes, rather than the percentage of dark material. As shown in Fig. 5 and Table 2, when increasing the percentage of dark components in BAS samples, no trend is observed within the experimental error. On the other hand, comparing the four different series, we observed a shift of the CF towards smaller wavelengths with increasing grain size. Considering the average value for each series, the CF shift of about 0.19 μm between grain sizes of <50 μm and 500–1000 μm. Comparing these results to the literature, we evaluate from Shirley & Glotch (2019), the average shift for pyroxene and feldspar of about 0.30 μm between samples with grain sizes of <32 μm and >250 μm (in detail, the average CF shift is 0.23 μm for pyroxene and 0.36 μm for feldspar within a range of shift from 0.09 μm to 0.74 μm). Our shift in the average values is 0.19 μm; this is perfectly in line when we consider that lower pressure used in Shirley & Glotch work (10^{-6} mbar) will increase the shift. Indeed, for comparison, the average CF shift for pyroxene and feldspar in air measured by Shirley & Glotch is 0.04 μm.

In the MIR range, we present the first analysis of variation of RB for samples at different grain sizes with an increasing percentage of dark material in this paper. Results are shown in Fig. 6. From panels A, B, C, and D, we can immediately observe as the decreasing grain size influences the spectral contrast (band intensity) of the sample. We would like to point out that the scale of panel A is different from the rest of the panels. We therefore make the observation that as grain size decreases, the intensity of RBs decreases with the appearance of TF for size <50 μm, in perfect agreement with the relevant literature (Le Bras & Erard 2003). Looking at the different trends that are due to the increasing percentage of amorphous carbon with each grain size, once again, we observe a general decreasing trend for RB. Figures 6E–I show the band area and peak intensity for the main peak of RB. Here, not all the grain sizes show a monotonic trend: in particular, small grain size samples present an initial increase when adding 1% of SAC and after a monotonic decrease. The same behavior with small differences is visible for the bigger grain sizes above 200 μm, the only series with a monotonic decrease is the 50–200 μm. We need to notice that RB is a feature extremely sensitive to mineralogical changes that can be induced by mixing of natural minerals. Yet still, a normal mixing of smaller grain sizes tends to be more homogeneous than mixing at larger grain sizes (as shown by smaller experimental errors); this, in fact, offers a confirmation of these trends. Moving to the TF shown in Fig. 7 we can see by looking at panel B how, once again, the RB calculated at 10.53 μm shows a similar trend to that of the RB at 8.89 μm, albeit more linear, while the TF follows a nonlinear, but definitely monotonic trend.

4.2. Consideration on remote sensing application

In attempting to apply these results to remote sensing interpretations, we take the opportunity to note some important points. The modification of the OH band when adding an increasing percentage of dark material is stronger than the modification of the RB. For smaller grain sizes, the OH band is already reduced by half with the addition of 10% in opaque material; on the other hand, the spectral contrast in the RB region is less reduced. This result could explain the absence of intense features in the NIR region for some very dark objects such as Phobos (Poggiali et al. 2022). This result is even more interesting considering recent findings on the intensity of OH shown by anhydrous material mixed with hyperfine hydrated mineral (Poggiali et al. 2023). Although the OH band present in the spectra of our samples is not related to a purely hydrated composition, taking into account the similarities obtained from similar works with hydrated minerals, we can hypothesize a more generic surface application characterized by a greater presence of hydrated material, but also by a very low albedo. In dark surfaces with a prominent 2.7 μm OH band such as Bennu (Hamilton et al. 2019) and Ryugu (Kitazato et al. 2019), with almost absent NIR features (Simon et al. 2020), the mixing of hydrated material could happen after the darkening of the surface. On the other hand, the minimal OH features observed on Phobos (Rivkin et al. 2002) do not rule out the presence of hydrated material, if the mixing with dark material happened at a later stage, thereby decreasing the spectral contrast.

Moreover, for compositionally homogeneous bodies, differences in the spectral contrast slope and the other features examined in this work can be influenced by the grain size and percentage of dark material in a non-linear way. In analyzing differences and similarities in our dataset, one of the most valid hypotheses that can be introduced is that bright grains with larger surface areas may harbor larger percentages of small dark grains before seeing the formation of clumps. Therefore, this dataset will serve as a valid tool to improve our knowledge on observed mixtures of bright and dark material across the Solar System and will be helpful for future observations. Actually, the mixing of different bright and dark material was already found on different bodies such as carbonaceous asteroids Ryugu (Tatsumi et al. 2021) and Bennu (DellaGiustina et al. 2021) as well as differentiated asteroid Vesta (Turrini et al. 2014), where carbonaceous dark material contamined a brighter surface due to impacts.

A good understanding on how different mixtures, particularly those with a peculiar microscopic appearance as small grains diffuse onto bigger grains, could be useful in linking the data collected on returned samples to remote sensing observations in the case of Ryugu (Pilorget et al. 2021; Dartois et al. 2023) and the next sample return missions. In closing, however, we must remark that the difficulties encountered in studying the spectroscopic nature of dark bodies in the Solar System comes from the multiple processes that can affect the surface of a rocky body that is not protected by an atmosphere. Several processes can be invoked to explain the spectroscopic aspect of the surface, with space weathering and thermal alteration figuring as two of the most probable among the rest. Although these processes are not taken into account in this paper, additional experiments are planned to investigate their effects.

5. Conclusions

We present a complete and in depth study of the modification on IR spectra from 1.25 to 25 μm induced by complex mixing of bright basaltic components with a dark carbonaceous material at different grain sizes ranging from <50 to 1000 μm. We prepared several series of samples and measured multiple spectra to identify useful trends in interpreting observations and to validate mathematical models. Some of the most important findings are as follows:

1. For percentages of dark material below 30–50%, the grain size of the bright component influences the reflectance

drastically. Above such quantities of dark material, the variation of absolute reflectance induced by big changes in grain size are strongly reduced;
2. Increasing the percentage of dark material produces a non-linear trend in the slope variation with a minimum value obtained with a certain percentage of dark material in the mixture, as observed in the literature. We discovered that the percentage of dark material needed to reach the minimum value in the slope is linked to the grain size of the bright component. Thus, a bigger size requires a higher percentage of dark material to induce the passage from a blueing trend to reddening trend;
3. The OH-stretching band around 2.7 μm shows a trend that is in agreement with previous literature results, although the switch between a linear and non-linear trend due to grain size variations of one of the components seems to be linked with a bigger dimension (200 μm) if the bright component is leading the grain size variation. Variations in the OH band depth in dark objects can also be related to the order of deposition of the hydrated and dark components;
4. The addition of dark material characterized by almost featureless spectrum in the MIR does not vary the position of Christiansen features, which (for homogenous samples) is driven by a change in grain size, as reported in previous works;
5. Reststrahlen band variations with a dark component show a variety of modification trends, with an increasing percentage of opaque material leading to a general monotonic decrease. The changes seem to be related to the mixing instead of possible compositional influences setting new constraints in mixture modeling. The Transparency feature trend for small grain sizes in a basaltic material mixture with amorphous carbon is different from the Reststrahlen band. This offers some hints on the different physical origins of the two bands;
6. Most of the changes observed in our dataset may support the hypothesis, as a preliminary analysis, that they are related to the scattering of dark grains on bright grains.

These findings not only expand our current knowledge of the mineral mixing of bright and dark materials but also – given the similarities with results obtained by other authors with different materials – they pose some constraints to the interpretation of IR data acquired on dark surfaces with different compositions, such as in the case of a carbonaceous asteroids Ryugu and Bennu. These objects were visited by the Hayabusa2 and OSIRIS-REx missions and the returned samples are available from those missions. Several present and past missions will also benefit from these results, such as Lucy (Levison et al. 2021), Juice (Grasset et al. 2013), JWST (Villanueva & Milam 2023), and MMX/MIRS (Kuramoto et al. 2022; Barucci et al. 2021). Moreover, we hope this new dataset can help in improving existing models for spectroscopic interpretation.

Acknowledgements. Authors want to thank Nathalie Ruscassier for the help with the SEM images acquisition and analysis. G.P., M.A.B., A.D. and A.W. acknowledge support by Centre National d'Etudes Spatiales (CNES). L.F. and J.R.B. acknowledge support from Italian Space Agency ASI-INAF agreement 2022-1-HH.0.

References

Arnold, G., & Wagner, C. 1988, Earth Moon Planets, 41, 163
Barucci, M. A., Reess, J.-M., Bernardi, P., et al. 2021, Earth Planets Space, 73, 211
Brown, A. J. 2014, Icarus, 239, 85
Brown, A. J., Calvin, W. M., McGuire, P. C., & Murchie, S. L. 2010, J. Geophys. Res. (Planets), 115, E00D13
Bruschini, E., Carli, C., Buellet, A. C., et al. 2022, Icarus, 378, 114950
Bussoletti, E., Colangeli, L., & Orofino, V. 1987, ApJ, 321, L87
Clark, R. N. 1983, J. Geophys. Res., 88, 10635
Clark, R. N., Curchin, J. M., Jaumann, R., et al. 2008, Icarus, 193, 372
Cloutis, E. A., Gaffey, M. J., Jackowski, T. L., & Reed, K. L. 1986, J. Geophys. Res., 91, 11 641
Cloutis, E. A., Gaffey, M. J., Smith, D. G. W., & Lambert, R. S. J. 1990, Icarus, 84, 315
Cloutis, E. A., Pietrasz, V. B., Kiddell, C., et al. 2018, Icarus, 305, 203
Colangeli, L., Mennella, V., Blanco, A., et al. 1993, ApJ, 418, 435
Cooper, C. D., & Mustard, J. F. 1999, Icarus, 142, 557
Dartois, E., Kebukawa, Y., Yabuta, H., et al. 2023, A&A, 671, A2
DellaGiustina, D. N., Kaplan, H. H., Simon, A. A., et al. 2021, Nat. Astron., 5, 31
DeMeo, F. E., & Carry, B. 2013, Icarus, 226, 723
Grasset, O., Dougherty, M. K., Coustenis, A., et al. 2013, Planet. Space Sci., 78, 1
Hamilton, V. E., Simon, A. A., Christensen, P. R., et al. 2019, Nat. Astron., 3, 332
Hasegawa, S., DeMeo, F. E., Marsset, M., et al. 2022, ApJ, 939, L9
Higuchi, A., & Ida, S. 2017, AJ, 153, 155
Hiroi, T., & Pieters, C. M. 1992, Lunar Planet. Sci. Conf. Proc., 22, 313
Hunt, G. R., & Vincent, R. K. 1968, J. Geophys. Res., 73, 6039
Hyodo, R., Genda, H., Charnoz, S., & Rosenblatt, P. 2017, ApJ, 845, 125
Kitazato, K., Milliken, R. E., Iwata, T., et al. 2019, Science, 364, 272
Kohout, T., Penttilä, A., Mann, P., et al. 2020, Planet. Sci. J., 1, 37
Kuramoto, K., Kawakatsu, Y., Fujimoto, M., et al. 2022, Earth Planets Space, 74, 12
Le Bras, A., & Erard, S. 2003, Planet. Space Sci., 51, 281
Levison, H. F., Olkin, C. B., Noll, K. S., et al. 2021, Planet. Sci. J., 2, 171
Lugassi, R., Ben-Dor, E., & Eshel, G. 2014, Geoderma, 213, 268
Milliken, R. E., & Mustard, J. F. 2007, Icarus, 189, 574
Mustard, J. F., & Hays, J. E. 1997, Icarus, 125, 145
Piatek, J. L., Hapke, B. W., Nelson, R. M., Smythe, W. D., & Hale, A. S. 2004, Icarus, 171, 531
Pieters, C. M., Fischer, E. M., Rode, O., & Basu, A. 1993, J. Geophys. Res., 98, 20817
Pilorget, C., Okada, T., Hamm, V., et al. 2021, Nat. Astron., 6, 221
Poggiali, G., Matsuoka, M., Barucci, M. A., et al. 2022, MNRAS, 516, 465
Poggiali, G., Iannini Lelarge, S., Brucato, J. R., et al. 2023, Icarus, 394, 115449
Pommerol, A., & Schmitt, B. 2008, J. Geophys. Res. (Planets), 113, E10009
Righter, K. 2007, Meteor. Planet. Sci., 42, 1039
Rivkin, A. S., Brown, R. H., Trilling, D. E., Bell, J. F., & Plassmann, J. H. 2002, Icarus, 156, 64
Salisbury, J. W., & Wald, A. 1992, Icarus, 96, 121
Salisbury, J. W., & Walter, L. S. 1989, J. Geophys. Res., 94, 9192
Salisbury, J. W., Walter, L. S., & Vergo, N. 1987, U.S. Geol. Surv., 87, 263
Salisbury, J. W., D'Aria, D. M., & Jarosewich, E. 1991, Icarus, 92, 280
Shirley, K. A., & Glotch, T. D. 2019, J. Geophys. Res. (Planets), 124, 970
Simon, A. A., Kaplan, H. H., Cloutis, E., et al. 2020, A&A, 644, A148
Sultana, R., Poch, O., Beck, P., Schmitt, B., & Quirico, E. 2021, Icarus, 357, 114141
Sultana, R., Poch, O., Beck, P., et al. 2023, Icarus, 395, 115492
Takir, D., Stockstill-Cahill, K. R., Hibbitts, C. A., & Nakauchi, Y. 2019, Icarus, 333, 243
Tatsumi, E., Sugimoto, C., Riu, L., et al. 2021, Nat. Astron., 5, 39
Turrini, D., Combe, J. P., McCord, T. B., et al. 2014, Icarus, 240, 86
Villanueva, G. L., & Milam, S. N. 2023, Nat. Commun., 14, 7444
Wargnier, A., Gautier, T., Poch, O., et al. 2023a, A&A, 669, A146
Wargnier, A., Poggiali, G., Doressoundiram, A., et al. 2023b, MNRAS, 524, 3809
Yang, B., Jewitt, D., & Bus, S. J. 2009, AJ, 137, 4538

Appendix A: Methods and additional figures

In this work, several spectral parameters were analyzed in a broad wavelength range spanning from NIR to MIR. All these parameters were evaluated independently using some Matlab routines coded in Arcetri laboratory and explained below. Moreover, using the OPUS software routines provided by Bruker, we validated the result obtained with our in-house built routine. Here, we summarize the method and procedures to evaluate all the selected features: the NIR slope, 2.7 μm OH-stretching intensity, position of the Christiansen feature (CF), and the variation in Reststrahlen band (RB) and Transparency feature (TF).

The NIR slope between $\lambda_1 = 1.5$ μm and $\lambda_2 = 2.5$ μm was evaluated using the formula from Wargnier et al. (2023a) converted to microns:

$$S = 10 \times \frac{R(\lambda_1) - R(\lambda_2)}{R(\lambda_1)(\lambda_1 - \lambda_2)} \ , \tag{A.1}$$

where R(λ) is the reflectance value at a wavelength, λ, and S is expressed as %100 μm. Results of the slope evaluation are reported in Figure 3 in the main text.

Thanks to the high resolution and an excellent signal-to-noise ratio (S/N), the position of the minima and maxima in the IR range under analysis could be identified by means of an automatic search of the minimum or maximum values in a selected range identified visually and larger than the features of interest. Some results were compared with OPUS results using a more precise center of gravity based algorithm with evaluation of the centroid of selected area. The comparison confirmed the goodness of a simple minima or maxima search in the particular case of our work. Moreover, the minima or maxima position that were critically involved in the evaluation of CF position were primarily the experimental error; this is due to the fact that the variability of the natural samples overrides the possible evaluation error given by the algorithm used.

To evaluate the intensity and and band area for the selected features we first set an approximate wavelength for the minimum or maximum of the features. It is important to remark that the positions of the features for OH, RB, and TF were not a subject of the analysis since no variation were observed (or expected) with the addition of the dark component, as for the CF. Therefore we used the same value for each spectrum at different percentage of a selected mixture series. For the OH-stretching band, we used the same position; while for the RB, we set different position for each mixture series at different grain sizes due to slight variations in the spectra. Each position used is reported in Table A.1.

Once the position of the features (either in the absorption band such as the 2.7 μm OH-stretching or features in MIR such as RBs) was set, we isolated the range and then divided it by a straight-line continuum, which was determined by two points shortward and longward of the features following standard analysis technique (Cloutis et al. 1986; Takir et al. 2019). The feature's intensity was evaluated as the difference between the spectrum in the minimum and maximum point and the evaluated continuum. Then, we performed a numerical integration of the features area via the trapezoidal method. This method approximates the integration over an interval by breaking the area down into trapezoids with more easily computable areas using the formula:

$$\int_a^b f(x)\,dx \approx \frac{b-a}{2N} \sum_{n=1}^{N} (f(x_n) + f(x_{n+1})). \tag{A.2}$$

Results of area integration and intensity evaluation was reported in this paper normalized to the first values of the series to make all samples comparable and study the relative variation in the spectrum for different mixes and grain sizes.

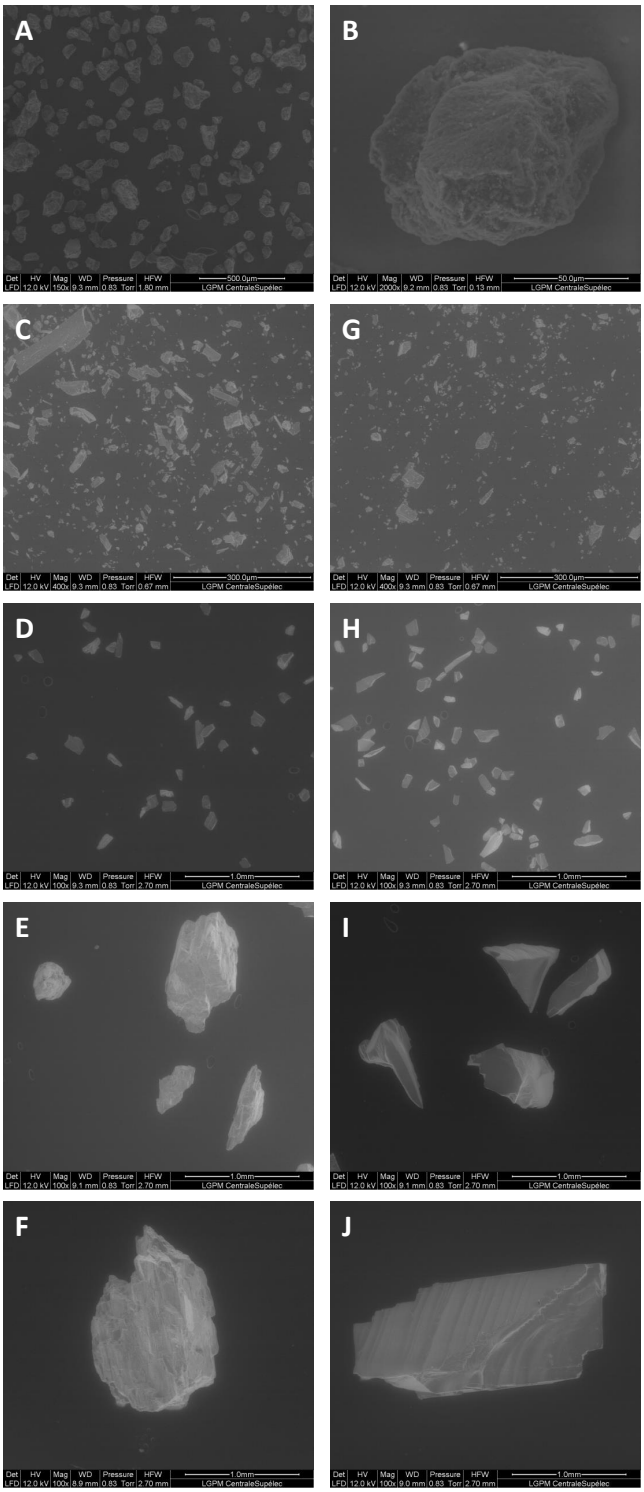

Fig. A.1. SEM images of the endmembers used in this work (shown from the top). Panels A and B: Synthetic amorphous carbon. Panels C to F: Images of different grain size samples of pyroxene augite and plagioclase bytownite. In detail: augite with grain sizes < 50 μm, 50-200 μm, 200-500 μm, 500-1000 μm is shown from top to bottom in panels C to F; bytwonite samples with grain sizes < 50 μm, 50-200 μm, 200-500 μm, and 500-1000 μm for are shown from top to bottom in panels G to J.

Sample series	Position OH [μm]	Limits for OH cont. [μm]	Position RB [μm]	Limits for RB cont. [μm]
BAS-A	2.7	2.66/3.28	8.89	8.11/14.8
BAS-B	2.7	2.66/3.28	8.90	7.9/15.16
BAS-C	2.7	2.66/3.28	8.81	7.96/15.16
BAS-D	2.7	2.66/3.28	8.84	7.96/15.16

Table A.1. Position of the RB peak

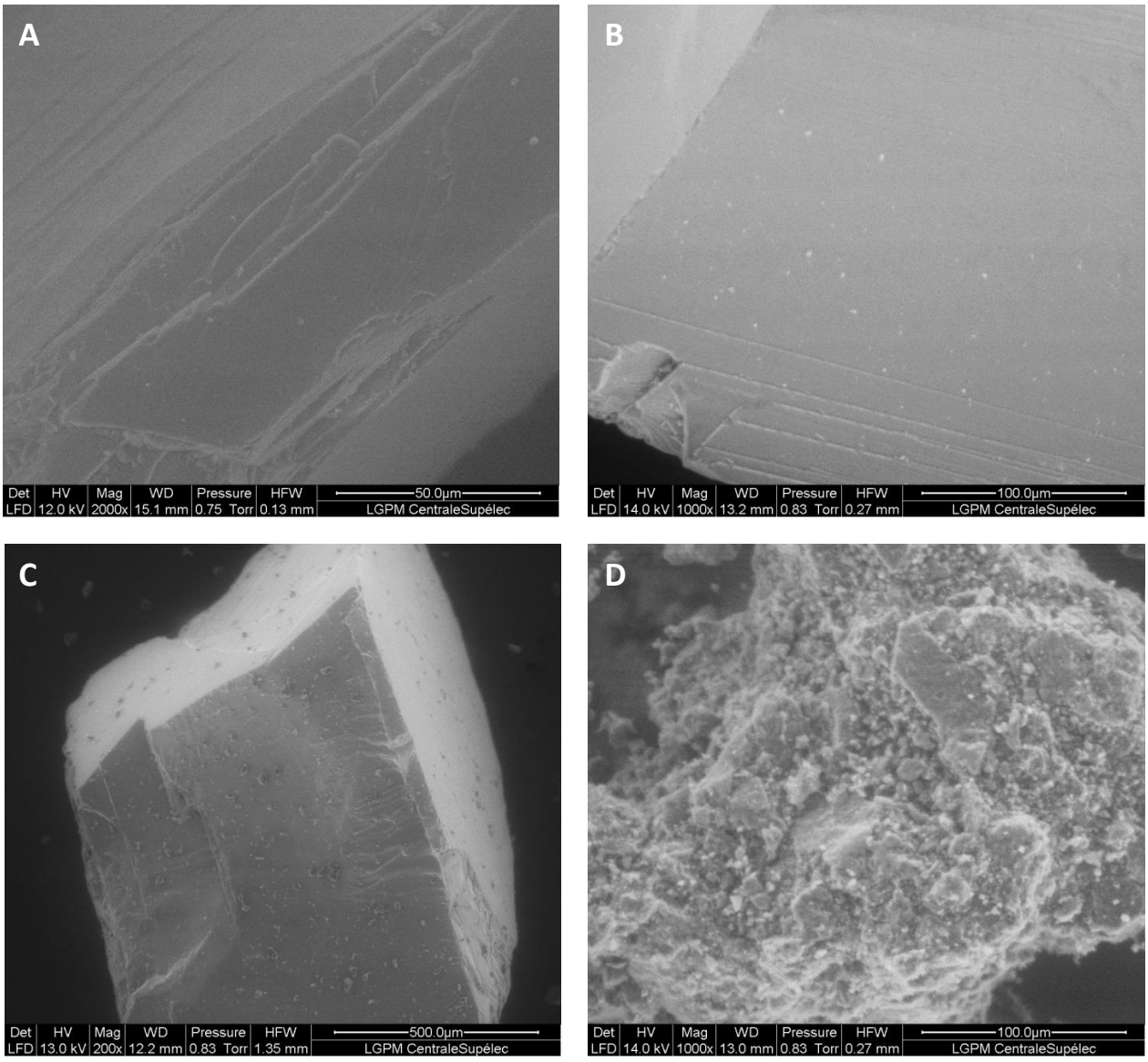

Fig. A.2. SEM images of some of the mixed sample prepared in this work. Panels A to D: Samples MIX-01C, MIX-02C, MIX-03D, and MIX-05B, respectively. The nominal percentage of SAC distributed on the bright grain surface increase is, respectively, 1%, 5%, 10%, and 50% among different samples. Spatial scale is not the same for all the images to shows the samples at different zoom levels.

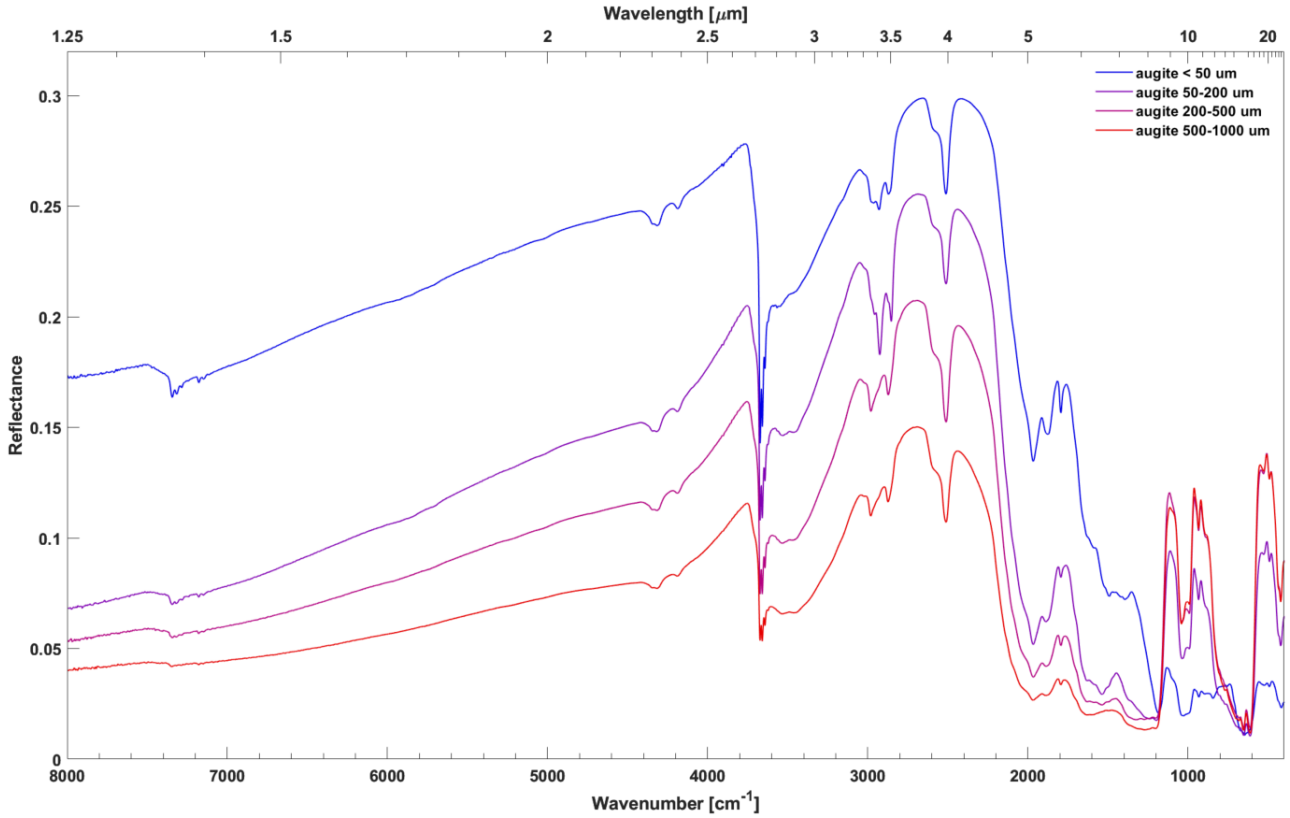

Fig. A.3. IR spectra of augite samples at different grain sizes (from top to bottom and from blue to red), respectively: <50 μm, 50-200 μm, 200-500 μm, and 500-1000 μm.

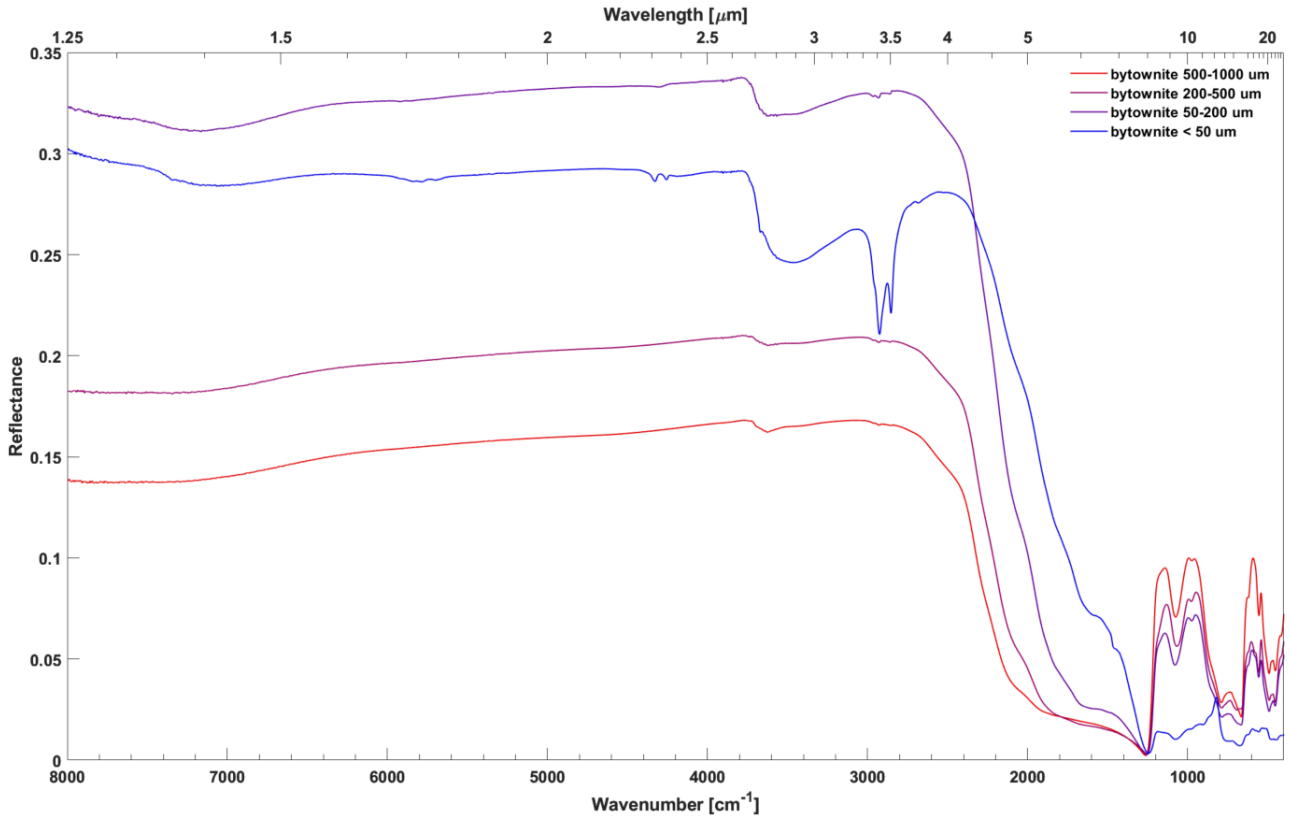

Fig. A.4. IR spectra of bytownite samples at different grain sizes from top to bottom (from blue to red) respectively: <50 μm, 50-200 μm, 200-500 μm, and 500-1000 μm.

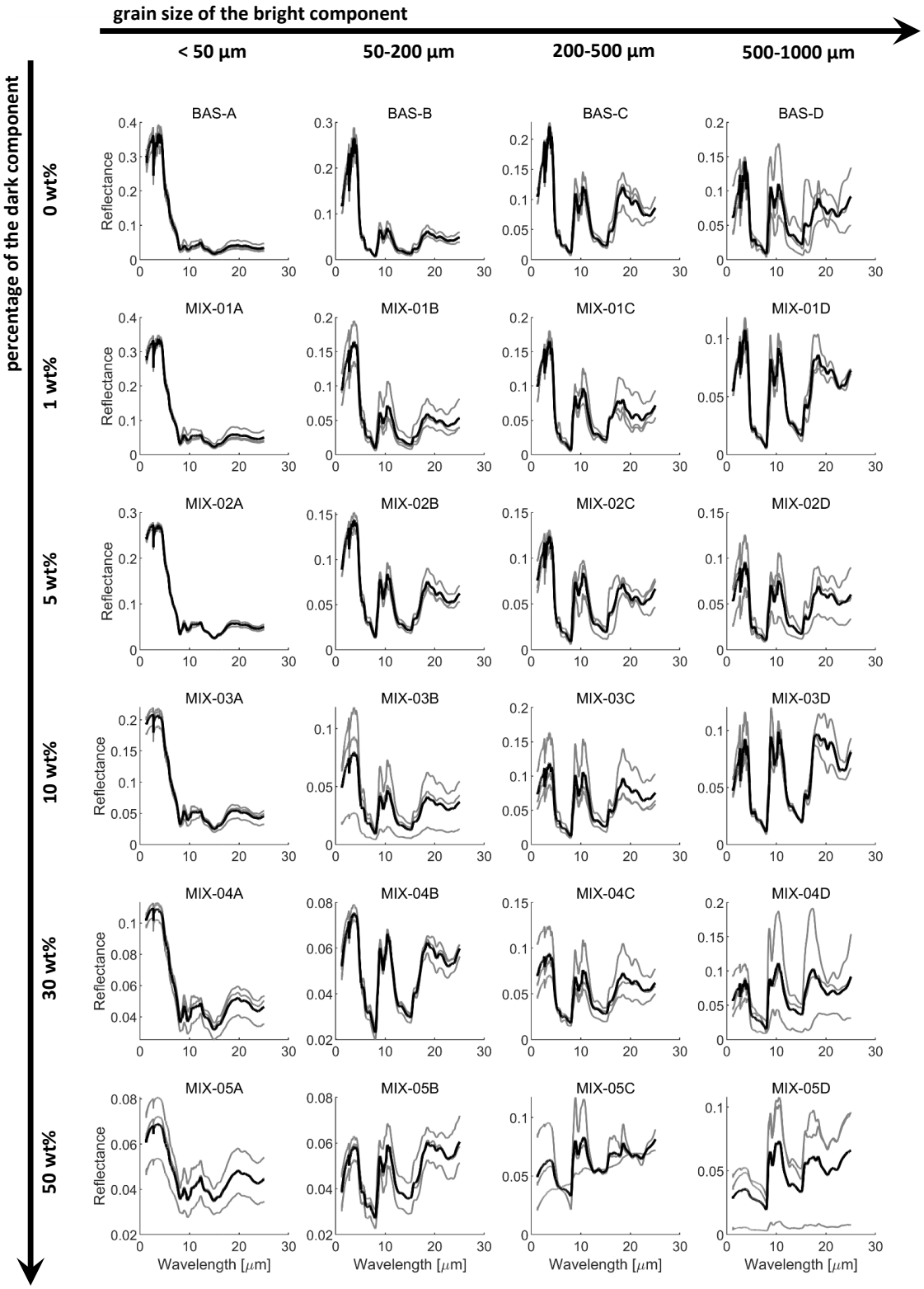

Fig. A.5. IR spectra of mixture samples at maximum and minimum scale for reflectance. For each mixture, three spectra were acquired and averaged to estimate the best spectrum.

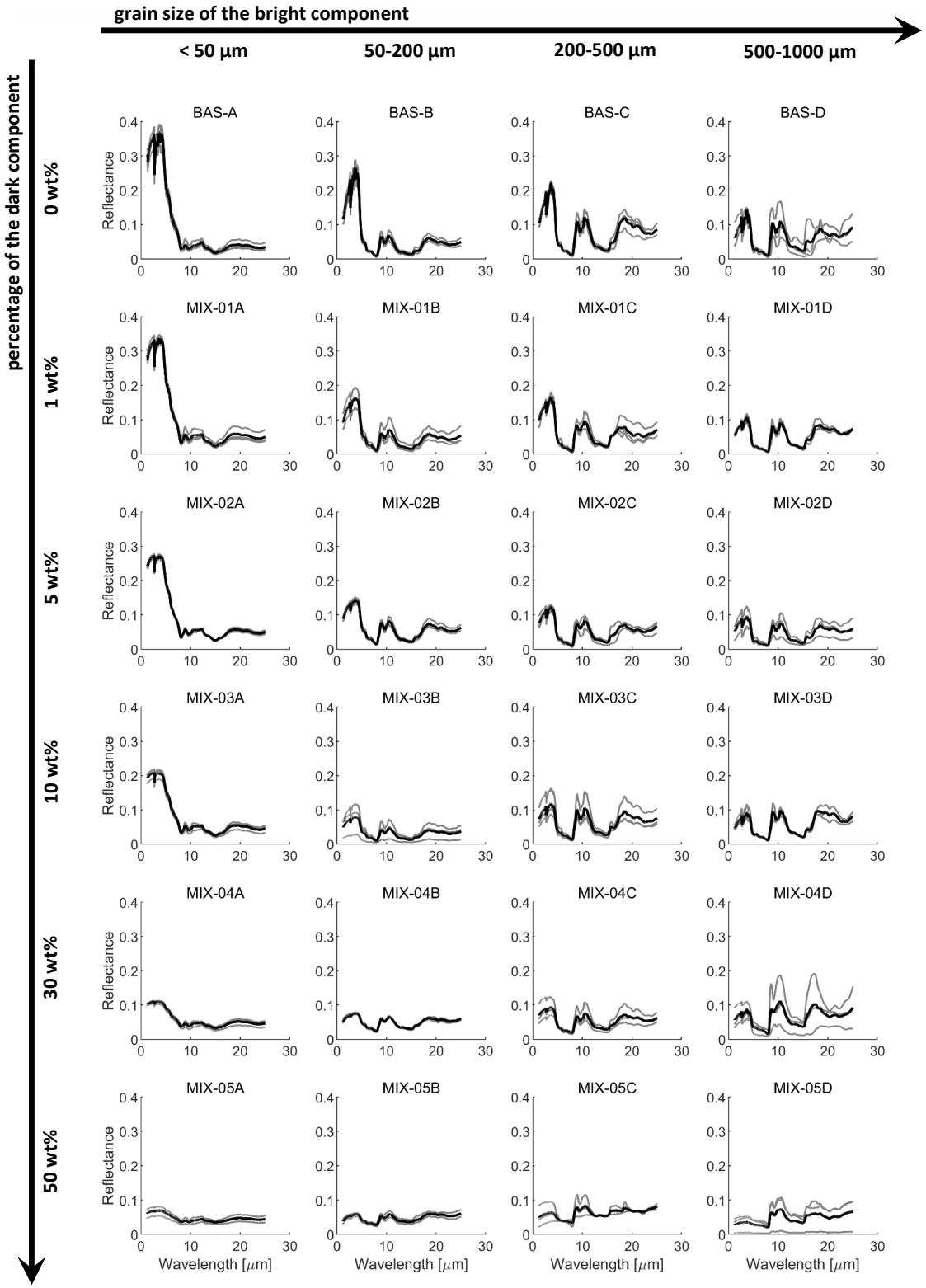

Fig. A.6. IR spectra of mixture samples at the same scale for reflectance. For each mixture, three spectra were acquired and averaged to estimate the best spectrum.

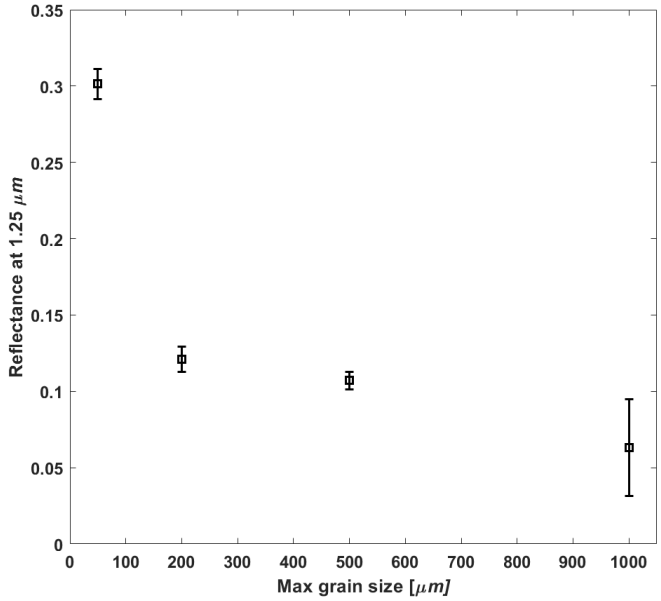

Fig. A.7. Reflectance at 1.25 μm for basaltic mixtures with different grain sizes. The grain size reported is the maximum grain size of the sample. The nominal ranges are: < 50 μm, 50-200 μm, 200-500 μm, and 500-1000 μm.